Channel Modeling for Orbital Angular Momentum Based Underwater Wireless Optical Systems

Lei Zhu, *Student Member, IEEE,* Haipeng Yao, *Senior Member, IEEE,* Jingjing Wang, *Senior Member, IEEE,* Qinghua Tian, Qi Zhang, *Member, IEEE,* Lajos Hanzo, *Life Fellow, IEEE*

***Abstract*—The underwater turbulence channel is modelled and a unified statistical distribution is applied for characterizing orbital angular momentum (OAM) propagation in underwater wireless optical communication (UWOC) systems. Based on Monte-Carlo simulations, the effects of turbulences are characterized by the multiple phase screens model considering both the coherence width and scintillation index. The phase screen samples are processed by the randomized spectral sampling discrete Fourier transform (DFT) technique. To validate the propagated field distribution, both the phase structure function and optical transfer function are derived and evaluated with the aid of ensemble-averaged results. The Generalized Gamma Distribution (GGD) enriched by an additional independent parameter is applied for modelling the probability density function (PDF) of both the reference-channels, fluctuating irradiance as well as the intermodal crosstalk irradiance between different OAM modes. Furthermore, based on the PDF, the performance metrics of both single input multiple output (SISO) and multiple input multiple output (MIMO) systems are analyzed, based on the average capacity, the bit-error rate and the outage probability.**

***Index Terms*—Underwater wireless optical communication (UWOC), orbital angular momentum, channel modeling, performance analysis.**

I. Introduction

This work was supported in part by National Natural Science Foundation of China (NSFC) under Grants 61605013, 61675033, 61727817, 61775237, 61835005, 61875016, 62021005, 62105026, in part by the China Postdoctoral Science Foundation under Grants 2020M680385. The work of Haipeng Yao was supported by the Artificial Intelligence and Smart City Joint Laboratory (BUPT-TGSTII) (B2020001), Future Intelligent Networking and Intelligent Transportation Joint Laboratory (BUPTCTTIC) (B2019007). This work of Jingjing Wang was supported by the Young Elite Scientist Sponsorship Program by CAST (Grant No. 2020QNRC001). L. Hanzo would like to acknowledge the financial support of the Engineering and Physical Sciences Research Council projects EP/P034284/1 and EP/P003990/1 (COALESCE) as well as of the European Research Council's Advanced Fellow Grant QuantCom (Grant No. 789028)(Corresponding author: Lajos Hanzo.)

L. Zhu, Q. Tian, Q. Zhang are with the School of Electronic Engineering, State Key Laboratory of Information Photonics and Optical Communications, Beijing Key Laboratory of Space-ground Interconnection and Convergence, Beijing University of Posts and Telecommunications, Beijing 100876, China, (Email: zhulei@bupt.edu.cn; tianqh@bupt.edu.cn; zhangqi@bupt.edu.cn).

H. Yao is with the State Key Laboratory of Networking and Switching Technology, Beijing University of Posts and Telecommunications, Beijing 100876, China (Email: yaohaipeng@bupt.edu.cn).

J. Wang is with the School of Cyber Science and Technology, Beihang University, Beijing 100191, China. (Email: drwangjj@buaa.edu.cn)

L. Hanzo is with the School of Electronics and Computer Science, University of Southampton, Southampton, SO17 1BJ, UK. (Email: lh@ecs.soton.ac.uk).

UNderwater optical wireless communication (UWOC) has attracted considerable attention in applications such as navigation, sensor networks, oceanographic studies and oil exploration [1]. However, both acoustic as well as radio frequency (RF) and optical waves have their own pros and cons. Given the disadvantages of limited bandwidth, higher power consumption and bulky transmitter construction of the existing acoustic and RF solutions, UWOC has found favour in many applications [2]. UWOC systems with a carrier wavelength operating in the blue-green region hold the promise of high data rates with the lowest attenuation in clear seawater [3].

Optical beams having a helical phase front carry orbital angular momentum (OAM). The beneficial extra spatial degree-of-freedom in OAM beams can be readily exploited for both multiplexing and modulation, hence dramatically increasing the channel capacity [4] explicitly, the mutual orthogonality of OAM modes directly increases the spectral efficiency [5]. Hence, OAM has been investigated both in classical and underwater quantum communication systems in the infrared and visible light region [6]. However, OAM beams are susceptible to turbulence-induced distortion in realistic underwater communication scenarios. The scintillations caused both by temperature fluctuations and salinity variations give rise to deep fading of the optical signal [7]. Furthermore, the phase front of OAM beams may suffer from severe distortion, resulting in considerable intermodal crosstalk among OAM modes [8].

The classic Monte-Carlo-based method may be adapted for constructing propagation models in the face of turbulences [9]. This technique can be realized by the popular split-step Fourier propagation based on multiple phase-screen models [10], while relying on the average of these random samples generated by Monte-Carlo simulations. Recently, multiple phase screen models based on the power spectrum inversion method of [11] have been applied for underwater turbulence channels [12]. However, the rules of incorporating phase screens are not well-established and each screen is independent. Naturally, a model may only be deemed adequate, if the experimental results match the analytical results. But the drawback of this method is that it is computationally cumbersome, since it involves large matrixes dimensions and an enormous number of iterations in different turbulence regimes. To circumvent this computational challenge, a statistical model is proposed to characterize the distribution of the optical irradiance signal fluctuations inferred from these random samples. Accordingly, the probability density function (PDF) of the randomly fluctuating irradiance can be deduced from the statistical model.

In the past, several statistical models have been proposed for the irradiance PDF expressions [13], [14]. For example, the mixture of the exponential-generalized Gamma and Fischer-Snedecor distributions have been used for characterizing the irradiance both in atmospheric [14] and underwater scenarios [13]. Recently, a variety of mathematically intractable statistical models have been conceived for optical OAM PDF relying on distribution fitting [15]–[17]. It was shown in [15] that the randomly fluctuating irradiance of OAM modes experienced in different atmospheric turbulence conditions it obeys the Johnson S_B distribution, where the linear-scale transformed distribution fits well with the experimental data. As a further development, a dual Johnson S_B statistical distribution is proposed in [16] for the reference-channel irradiance of the OAM propagation model. Furthermore, the Generalized Gamma distribution (GGD) has been proposed as a mathematically tractable alternative model for the crosstalk in the face of the fluctuating irradiance as well as of the intermodal crosstalk irradiance of OAM modes in a wide range of atmospheric turbulence conditions [17].

However, to the best of our knowledge, there is no comprehensive multiplane-transmit model in the open literature for statistically characterizing the fluctuating irradiance of optical OAM in UWOC systems. In this paper, the underwater turbulence model is established by using a Monte-Carlo simulation based framework for generating random phase screens of the transmission model. The coherent width and the scintillation index of the plane wave are used both for characterizing the underwater turbulence conditions as well as the required phase screen properties along the propagation path. The phase screens are generated by the discrete Fourier transform (DFT) method [11] and the numerical results are compared to the corresponding analytical solutions. The GGD associated with an additional independent parameter is proposed for accurately matching the PDF of the crosstalk of the fluctuating irradiance and intermodal crosstalk irradiance between OAM modes of different turbulence regimes. The maximum likelihood estimation (MLE) technique is applied for obtaining the parameters of the GGD. In order to validate the superiority of the GGD model, the root mean square error (RMSE) of the cumulative density function (CDF) is compared to the Johnson S_B, Gamma, dual Johnson S_B and Exponential distributions defined in [17] under various turbulence conditions. Both single-input single-output (SISO) and multi-input multi-output (MIMO) systems are considered, which are based on intensity modulation and direct detection (IM/DD). Our objective is to derive mathematically tractable expressions of the average capacity, the BER and the outage probability. At the receiver, the classic maximum ratio combining (MRC) technique is used. In a nutshell, our novel contributions are boldly and explicitly contrasted to the literature in Table I. It can be observed from the Table I that this is the first time that our paper investigates the average irradiance accuracy of OAM beams in underwater environment, as well as analyzes the performance analysis of the MIMO scenario in OAM-based UWOC system.

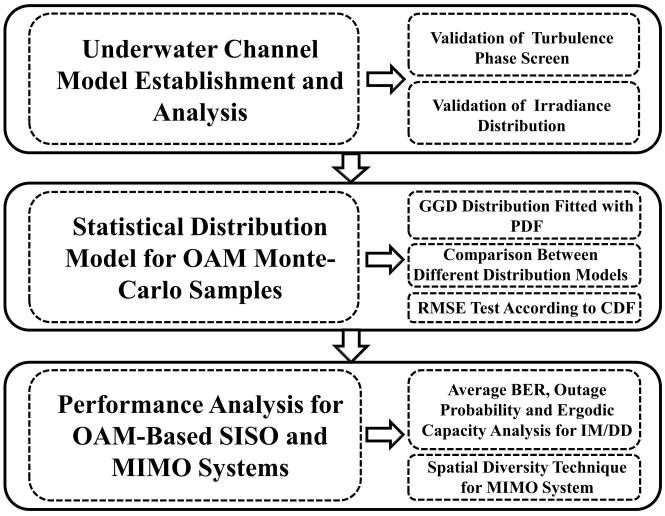

Fig. 1. The structure of this treatise

The remainder of this paper is organized as seen in Fig. 1. In Section II, the OAM propagation model based on Monte-Carlo simulations is constructed for the UWOC system considered. In Section III, the GGD model associated with an additional independent parameter is proposed and fitted to the simulated PDF. The results of the GGD are compared to the dual Johnson S_B, Gamma, dual Johnson S_B and Exponential distributions under various turbulence conditions. In Section IV, the performance of our OAM-based UWOC system relying on both SISO and MIMO links is investigated. Finally, in Section V, we offer our conclusions.

II. SYSTEM AND CHANNEL MODELS

A. Orbital Angular Momentum Communication System

In classical communication systems, a lightwave carrying an OAM of $m\hbar$ per photon is a wave with twisted phase-front $\exp(il\varphi)$, where $\hbar$ is the reduced Planck constant, l is an unbounded integer labeled as topological charge and φ is defined as the azimuth [22]. Laguerre-Gauss (LG) beams have been regarded as a special subset among OAM beams, which have been widely used for optical communication [5]. For LG beams, the azimuthal and radial wavefront distributions are defined as two indices, l and p respectively, and the spatial distribution of the optical field in turbulence-free environment can be expressed as [22]

$$u_{p,l}(\rho,\varphi,z) = \sqrt{\frac{2p!}{\pi(p+|l|)!}}\frac{1}{\omega(z)}\left[\frac{\rho\sqrt{2}}{\omega(z)}\right]^{|l|}\exp\left[\frac{-\rho^2}{\omega^2(z)}\right] \times L_p^{|l|}\left[\frac{2\rho^2}{\omega^2(z)}\right]\exp\left[\frac{-ik\rho^2 z}{2\left(z^2+z_R^2\right)}\right] \times \exp\left[i(2p+|l|+1)\tan^{-1}\left(\frac{z}{z_R}\right)\right]\exp(-il\varphi), \quad (1)$$

where (ρ,φ) represents the polar coordinates in a plane perpendicular to the propagation direction of the z axis, where $z=0$ represents the vertical transmit plane and $z=L$ corresponds to the received plane. Furthermore, $w(z) = w(0)\left[\left(z^2+z_R^2\right)/z_R^2\right]^{1/2}$ stands for the $1/e$ radius of the

TABLE I
COMPARISON OF RELATED WORK ABOUT OAM IN FSO AND UWOC SYSTEMS

Novelty and Related Works		Our Paper	2013 [18]	2015 [15]	2016 [19]	2017 [20]	2019 [21]	2019 [16]	2020 [17]	2020 [12]
Channel Model	Phase Structure Fuction Accuracy	✓								✓
	Scintillation Index	✓	✓	✓	✓	✓	✓	✓	✓	✓
	One Hop	✓	✓	✓	✓	✓	✓	✓	✓	✓
	Dual Hop						✓			
	Average Irradiance Accuracy	✓			✓					
Performance Analysis	OAM Mode Purity	✓			✓			✓		✓
	Space-Time Coding					✓			✓	
	Outage Probability	✓					✓		✓	
	BER	✓	✓			✓	✓		✓	✓
	Ergodic Capacity	✓					✓		✓	
	MIMO with Different Data	✓								
	Spatial Diversity	✓				✓			✓	
	Fiber Couple Efficiency			✓	✓					
	MSE or RMSE	✓	✓				✓		✓	
	Intensity Modulation/Direct Detection	✓	✓			✓	✓		✓	✓
	Hererodyne Detection						✓			
	Channel Estimation			✓		✓				
	Probability Density Function	✓	✓	✓			✓	✓	✓	
	Cumulative Density Function	✓					✓	✓	✓	

Gauss term, where $w(0)$ is the beam waist, $z_R = \pi w(0)^2/\lambda$ is the Rayleigh range, and $(2p+|l|+1)\tan^{-1}(z/z_R)$ is the Gouy phase. Finally, $L_p^{|l|}(x)$ is an associated Laguerre polynomial, obtained from the more familiar Laguerre polynomials formulated as:

$$L_p^{|l|}(x) = (-1)^{|l|}\frac{d^{|l|}}{dx^{|l|}}L_{p+|l|}(x). \tag{2}$$

In this contribution, the LG modes having $l > 0$ and $p = 0$ will be considered in defining the OAM-based UWOC system.

Given the orthogonality of the OAM modes as they propagate through a perfect channel under turbulence-free conditions, the reference-channel mode will be preserved and the desired relationship between different OAM modes will be satisfied as

$$\int u_{p,l}(\boldsymbol{\rho},z)u^*_{p,m}(\boldsymbol{\rho},z)d\boldsymbol{\rho} = \begin{cases} I_l, & \text{if} \quad l = m \\ 0, & \text{if} \quad l \neq m \end{cases}, \tag{3}$$

where $u_l(\boldsymbol{\rho},z)$ denotes complex optical field associated with the distribution of order l at the distance z, while I_l represents the power of the LG beams.

In Fig. 2, an OAM UWOC transmission system is represented. At the transmitter, the laser relying on an amplitude modulator (AM) generates the modulated signal for the OAM beams. More specifically, we could directly obtain a single or superposed OAM beam by passing a Gaussian beam through spatial light modulators (SLM) [23]. The SLMs create the desired OAM modes associated with specific holograms and the single or multiplexed LG beams with twisted phase distributions are then transmitted through the underwater channel constructed by predesigned random multi-phase screens. At the receiver, the channel-impaired LG beams will be detected relying on the conjugate holograms loaded onto the SLMS. The detected optical beams are then converted to the corresponding electrical signal by avalanche photodiodes (APD).

B. OAM Propagation Through Monte-Carlo-Based Underwater Turbulence

Turbulence-induced scintillation causes deep random fading, thus destroying the orthogonality of different OAM modes. A common technique of modelling channel turbulences is to treat them as a finite number of discrete layers [24]. The model could be designed and verified in terms of the resultant power spectral density (PSD), scintillation properties and coherence diameter. In what follows, firstly, the phase screens are generated and characterized in terms of their phase structure functions (PSF); subsequently, based on the results obtained, Monte-Carlo-based techniques may be used for generating instantiations of the underwater turbulence channel; finally, the average irradiance distribution of LG beams is compared to the analytical formulae for the validation of the numerical results.

1) Generations of Phase Screens: The pure phase perturbations can be realized by phase screens originally introduced in the seminal contribution of [9]. Various techniques have been proposed for the generation of random phase screens in [25], The most popular method is based on employing the inverse Fourier transform, where the phase of the complex PSD is deduced from that of the refractive-index. The underwater spatial fluctuations of the refractive-index obeys the Nikishov spectrum designed in [26] and formulated as:

$$\begin{aligned}\Phi_n(\kappa) = 0.388\cdot 10^{-8}\varepsilon^{-1/3}\kappa^{-11/3}\left[1+2.35(\kappa\eta)^{2/3}\right] \\ \times \frac{X_T}{w^2}\cdot\left(w^2 e^{-A_T\delta}+e^{-A_{TS}\delta}-2e^{-A_S\delta}\right),\end{aligned} \tag{4}$$

where the experimental constants are $A_T = 1.863\cdot 10^{-2}, A_S = 1.9\cdot 10^4, A_{TS} = 9.41\cdot 10^{-3}, \delta = 8.284(\kappa\eta)^{\frac{1}{3}} + 12.978$. Furthermore, κ is the spatial frequency, ε is the rate of dissipation of the kinetic energy per unit mass of fluid ranging from $10^{-1}\mathrm{m}^2/\mathrm{s}^3$ to $10^{-10}\mathrm{m}^2/\mathrm{s}^3$, X_T is the dissipation rate of the mean-squared temperature varying from $10^{-4}\mathrm{K}^2/\mathrm{s}$

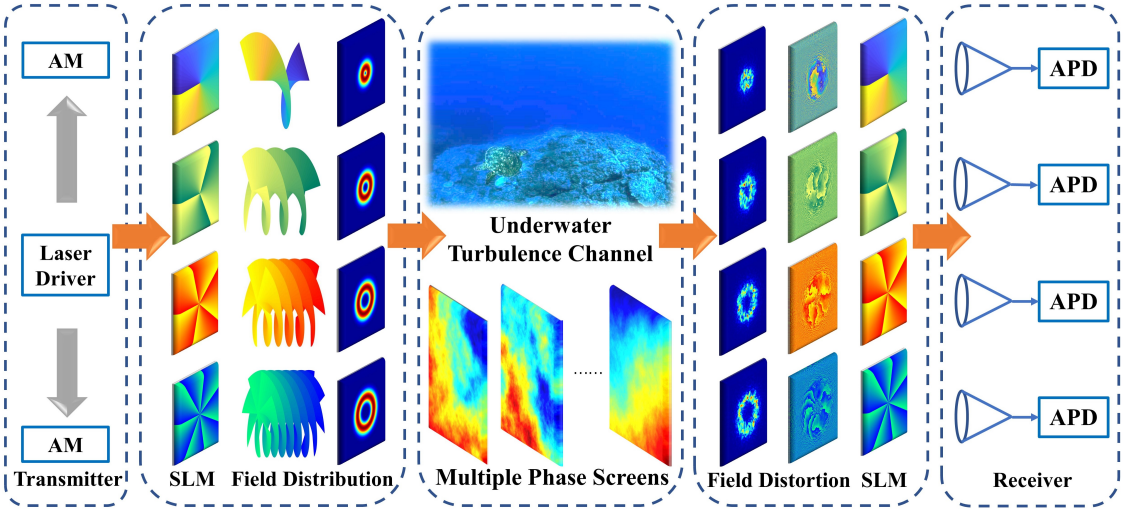

Fig. 2. An OAM UWOC system showing the transmitter, channel model and receiver. (AM: Amplitude Modulator, SLM: Spatial light modulator, APD: Avalanche Photodiode.)

to $10^{-10}\mathrm{K}^2/\mathrm{s}$ in clean sea-water and η is the Kolmogorov microscale length. Still referring to Eq. (4), w denotes a unitless parameter specifying the ratio of temperature and salinity contributions to the refractive spectrum that varies from -5 to 0. The values of -5 and 0 correspond to the dominant temperature-induced and salinity-induced underwater turbulence, respectively [27]. The relationship between the phase PSD and refractive-index PSD can be described as

$$\Phi_\phi(\kappa) = 2\pi k^2 \Delta z \Phi_n(\kappa), \tag{5}$$

where Δz denotes the propagation distance between the subsequent phase screens. The SH correction for the phase screen achieved by DFT-based uniform spatial sampling method has been widely used. Although, the DFT-based SH correction method of [28] has indeed provided more accurate phase samples, it still suffers from some disadvantages in the generation of phase screens. The DFT-SH-based randomized spectrum sampling method proposed by Paulson, Wu and Davis (PWD) [29] may also be applied for alleviating the low-frequency deficiency of the DFT. The resultant complex phase screen can be described as:

$$\psi_{\mathrm{PWD}}(j\Delta x, h\Delta x) = \sum_{m,n=-N_{\mathrm{PWD}}/2}^{N_{\mathrm{PWD}}/2-1} a_{m,n}^{\mathrm{PWD}} \times \exp\left(\frac{2i\pi}{N_{\mathrm{PWD}}}\left[(m+\xi)j + (n+\zeta)h\right]\right), \tag{6}$$

where ξ and ζ are independent and identically distributed (i.i.d.) random variables within the interval $(-0.5, 0.5)$.

Additionally, the SH components are realized relying on the random sampling method for the mitigation of the low-frequency deficiency of the phase samples, which can be formulated as [29]:

$$\psi_{\mathrm{SH}}^{\mathrm{PWD}}(j\Delta x, h\Delta x) = \sum_{p=1}^{N_{\mathrm{SH}}} \sum_{m,n=-1}^{1} a_{p,m,n}^{\mathrm{PWD}} \left(1 - \delta_{m,0}\delta_{n,0}\right) \times \exp\left[\frac{2i\pi}{3^p N_{\mathrm{PWD}}} j\left(m + \xi_{p,m,n}\right) + h\left(n + \zeta_{p,m,n}\right)\right] + a_{N_{\mathrm{SH}},0,0}^{\mathrm{PWD}} \exp\left[\frac{2i\pi}{3^{N_{\mathrm{SH}}} N_{\mathrm{PWD}}}\left(j\xi_{N_{\mathrm{SH}},0,0} + h\zeta_{N_{\mathrm{SH}},0,0}\right)\right]. \tag{7}$$

Similarly, the variables $\xi_{p,m,n}$ and $\zeta_{p,m,n}$ are i.i.d. $U(-0.5, 0.5)$ random variables. Furthermore, the coefficient $a_{m,n}^{\mathrm{PWD}}$ and the random complex coefficient $a_{p,m,n}^{\mathrm{PWD}}$ were derived in [29].

To evaluate the accuracy of phase screens, the PSF is derived and compared to a series of simulated phase samples. Due to the finite number of samples, any target structure function will be biased with respect to the simulated samples, thereby resulting in sampling error. The analytical formulations of PSF associated with an unbounded plane wave in underwater environment can be expressed as [24]

$$D_{psf}^{pw}(\rho, z = L) = 4\pi^2 k^2 L \int_0^1 \int_0^\infty \kappa \Phi_n(\kappa) \left[1 - J_0(\kappa\rho)\right] \times \left\{1 + \cos\left[\frac{L\kappa^2\xi}{k}\right]\right\} \mathrm{d}\kappa \mathrm{d}\xi, \tag{8}$$

where $J_0(\cdot)$ denotes zero-order Bessel function and L is the propagation path length. In the case of $\rho \gg \eta$, the PSF can be expressed as [30, eq. (7)]

$$D_{psf}^{pw}(\rho, z = L) \approx \varepsilon^{-1/3}\left(\chi_T / w^2\right)\rho^{5/3}\left[3.063 \times 10^{-7} \times k^2 L\left(1.116w^2 - 2.235w + 1.119\right) - L^3\left(1.841w^2 - 40.341w + 2077\right)\right]. \tag{9}$$

The structure function may also be considered as a statistic measurement of random fields and the corresponding expressions can be defined as [11, eq. (3.25)]

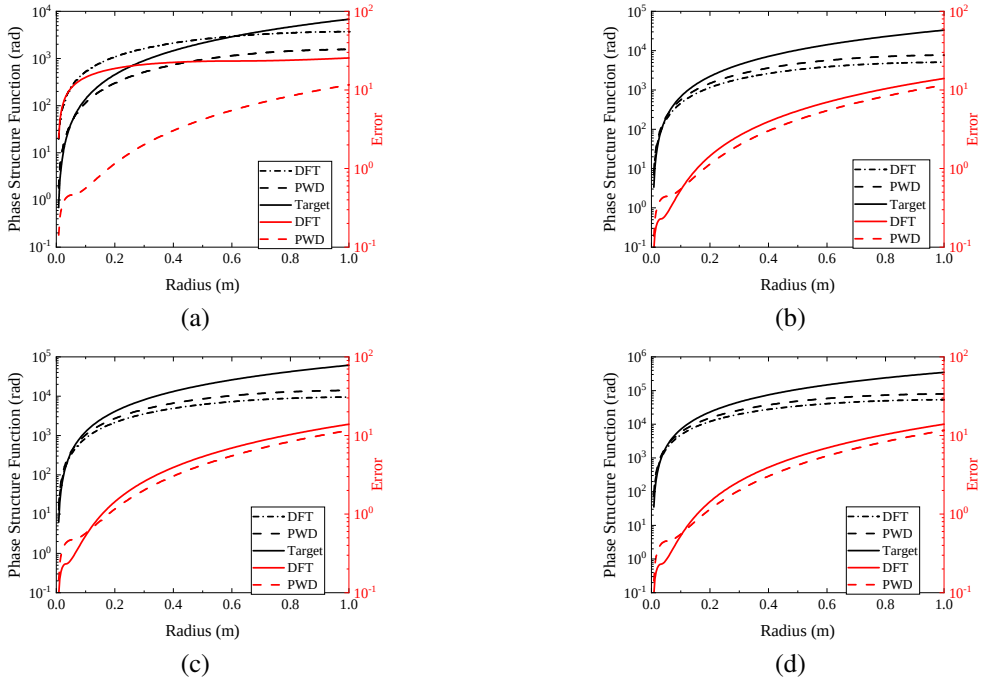

Fig. 3. Comparison of the phase samples, PSF based on two different methods of mitigating low-frequency deficiency versus results from the theoretical formulation of Eq. (6) and Eq. (7) using 1024×1024 grid points. The RMS error as a percentage relative to theory over 20,000 phase screens trials in three different turbulence strength classified as (a)$\sigma_R^2 = 0.1$, (b)$\sigma_R^2 = 0.8$, (c)$\sigma_R^2 = 1.2$ and (d)$\sigma_R^2 = 2.4$

$$D(\triangle\boldsymbol{\rho}) = \langle[\psi(\boldsymbol{\rho}) - \psi(\boldsymbol{\rho}+\triangle\boldsymbol{\rho})]^2\rangle = 2\mathcal{F}^{-1}\left\{\mathrm{Re}\left[\mathcal{F}\left(\psi^2(\boldsymbol{\rho})\right)\mathcal{F}^*(\phi(\boldsymbol{\rho}))\right] - |\mathcal{F}(\psi(\boldsymbol{\rho}))|^2\right\}, \tag{10}$$

where $\psi(\boldsymbol{\rho})$ represents random samples of the phase screens and $\phi(\boldsymbol{\rho})$ denotes the matrix model with all one [11], while $\mathcal{F}$ is the Fourier transform. The root mean square (RMS) metric on the x axis and y axis are defined below as

$$\mathcal{E}_x = \sqrt{\frac{2}{M}\sum_{j=1}^{M/2}\left(\frac{D_x(j\Delta x) - D_{psf}^{pw}(j\Delta x)}{D_{psf}^{pw}(j\Delta x)}\right)^2}, \tag{11}$$

$$\mathcal{E}_y = \sqrt{\frac{2}{M}\sum_{l=1}^{M/2}\left(\frac{D_y(l\Delta y) - D_{psf}^{pw}(l\Delta y)}{D_{psf}^{pw}(l\Delta y)}\right)^2}, \tag{12}$$

$$\mathcal{E} = 100\% \times (\mathcal{E}_x + \mathcal{E}_y)/2, \tag{13}$$

where D_x and D_y are ensemble-averaged $x-$direction and $y-$direction sampled points gleaned from the structure function, while D_{psf}^{pw} is the target structure function value obtained from Eq. (9).

For characterizing the underwater turbulence intensity, the Rytov variance of plane waves is proposed, which is defined as [31, eq. (26)]

$$\sigma_R^2 = 8\pi^2 k^2 L \int_0^1\int_0^\infty \kappa\Phi_n(\kappa)\left[1 - \cos\left(\frac{L\kappa^2}{k}\xi\right)\right]\mathrm{d}\kappa\mathrm{d}\xi \approx 3.063\cdot 10^{-7}k^{7/6}L^{11/6}\varepsilon^{-1/3}X_T/w^2 \times \left(0.358w^2 - 0.725w + 0.367\right). \tag{14}$$

The turbulence intensity is usually classified according to $\sigma_R^2 < 1$ and $\sigma_R^2 > 1$ as weak and strong turbulence, respectively [32]. Our Monte-Carlo simulation results over 20,000 complex phase screens relying on both the DFT-SH-based and PWD-SH-based method are shown in Fig. 3. The theoretical PSF is also displayed as a target for the convenience of comparison. Furthermore, the RMS error between the numerical and theoretical simulations are shown as well. The phase screen size is set as $1\mathrm{m} \times 1\mathrm{m}$ and the number of grid points is 1024×1024. The inner scale is $\eta = 0.1\mathrm{mm}$, $N_{\mathrm{SH}} = 4$, the propagation distance is set to $L = 50\mathrm{m}$ and the wavelength is $\lambda = 532\mathrm{nm}$. The turbulence intensities are set to $\sigma_R^2 = 0.1$, $\sigma_R^2 = 0.8$, $\sigma_R^2 = 1.2$ and $\sigma_R^2 = 2.4$ for four different levels. As seen in Fig. 3, there is a gap between the target PSF and the one derived from random samples, especially at larger separations. This is because having a limited number of samples and using a simplified integration approach contribute to the differences between the numerical and analytical results. The PWD-SH-based method exhibits a better fit than the DFT-SH-based method. In contrast to the DFT-SH-based method, the PWD method generates non-periodic samples in the Fourier domain based on a frequency shift having practically unlimited size, while preserving the desired local statistics at the suggested scale [25]. Moreover, the randomly sampled SH components complement the PWD phase in the low-frequency spectral domain by using independent and approximately log-uniformly distributed points [33]. Hence, the unbiased phase samples obtained from the PWD-SH-based method provide more accurate approximation than the DFT-SH.

2) Propagation Model Based On Multiple Phase Screens: In order to characterize the propagation of LG beams in underwater turbulence environments, a multiple phase screen model is developed for the channel. Each layered model is

established based on the PWD-SH method discussed above, whose PSD and scintillation index match the corresponding extended medium. For a plane wave, the underwater spatial coherence width is an important parameter characterizing the structure function and PSD, which has a relationship with the coherence radius defined as [34, eq. (10)]

$$\begin{aligned} r_0^{pw} &= 2.1\rho_0^{pw} \\ &= \left[0.5846 \cdot 10^{-7} k^2 L X_T \varepsilon^{-\frac{1}{3}} w^{-2} \left(w^2 + 1 - 2w\right)\right]^{-\frac{3}{5}}. \end{aligned} \tag{15}$$

Then the phase PSD in Eq. (5) can be modified as

$$\begin{aligned} \Phi_\phi(f) = 0.0195 r_0^{-5/3} f^{-11/3} \left[1 + 8.0018(f\eta)^{2/3}\right] \\ \times \left(w^2 - 2w + 1\right)^{-1} \left(w^2 e^{-A_r \delta} + e^{-A_s \delta} - 2e^{-A_B \delta}\right), \end{aligned} \tag{16}$$

where f is the ordinary frequency in cycles/m. In order to determine r_0 of Eq. (15) for each phase screen in the propagation path, the effective coherence width of i^{th} layer is derived as

$$r_{0i} = \left[0.5846 \cdot 10^{-7} k^2 X_T \varepsilon^{-\frac{1}{3}} w^{-2} \left(w^2 + 1 - 2w\right) \Delta z_i\right]^{-\frac{3}{5}}. \tag{17}$$

Therefore, the coherence width of the plane wave for the entire transmission path can be expressed as

$$r_0^{pw} = \left[\sum_{i=1}^{n} r_{0i}^{-5/3}\right]^{-3/5}. \tag{18}$$

For the sake of approximating the turbulence intensity of each phase screen, the scintillation index is introduced, which is expressed as

$$\sigma_{I,pw}^2 = \sigma_{I,r}^2 + \sigma_{I,l}^2, \tag{19}$$

where $\sigma_{I,r}^2$ and $\sigma_{I,l}^2$ represent the radial and longitudinal components, respectively [35]. For the plane wave, the radial component of scintillation vanishes and the longitudinal component as a function of r_{0i} will be simplified to

$$\begin{aligned} \sigma_{I,pw}^2 \approx L^2 \sum_{i=1}^{n} r_{0_i}^{-5/3} \left(1 - \frac{z_i}{L}\right)^{5/6} k^{-2} \left(w^2 + 1 - 2w\right)^{-1} \\ \times \left(11.6007 \cdot 10^7 w^2 - 6.6994 \cdot 10^8 w + 13.0274 \cdot 10^{10}\right). \end{aligned} \tag{20}$$

Additionally, the scintillation index related to the inter-screen distance should be less than 10% of the total value [36]. Accordingly, the coherence width of each phase screen can be derived based on Eq. (18) and Eq. (20) by using the functions fmincons in the Optimization Toolbox of MATLAB and the underwater phase screens can be generated according to Eq. (6), Eq. (7) and Eq. (16). The phase screens are incorporated into the split step Fourier transform method of [37].

To validate the field distribution of the transmitted beam, the ensemble-averaged irradiance distributions of the propagated LG Beams gleaned from 20,000 samples are compared to the analytical results as described in [19]. The theoretical formulae of the ensemble-averaged irradiance of the LG beam propagating through underwater turbulence environments can be expressed as [19, eq. (14)], [38]

$$\begin{aligned} \langle I_l(\boldsymbol{\rho}, z = L)\rangle = \mathscr{F}^{-1}\{\mathscr{F}\left\{u_l(\boldsymbol{\rho}, z = L) u_l^*(\boldsymbol{\rho}, z = L)\right\} \\ \times \mathscr{F}\{\eta(\boldsymbol{\rho}, z = L)\}\}, \end{aligned} \tag{21}$$

where $\eta(\cdot)$ is the turbulence point spread function and $\mathscr{F}\{\eta(\cdot)\}$ denotes the optical transfer function (OTF), which can be viewed as the frequency response of the system relying on the expression of

$$\mathscr{F}\{\eta(\boldsymbol{\rho}, z = L)\} = \exp\left[-\frac{1}{2} D_{wsf}^{pw}\left(\kappa \frac{L}{k}\right)\right], \tag{22}$$

where $D_{wsf}^{pw}(\cdot)$ represents the wave structure function (WSF) of the plane wave formulated as [34, eq. (9)]

$$\begin{aligned} D_{wsf}^{pw}(\rho, z = L) &= 8\pi^2 k^2 L \int_0^\infty \kappa \left[1 - J_0(\kappa\rho)\right] \Phi_n(\kappa) \mathrm{d}\kappa \\ &\approx 3.603 \times 10^{-7} k^2 L \varepsilon^{-1/3} \chi_T w^{-2} \rho^{5/3} \\ &\times \left(1.116w^2 - 2.235w + 1.119\right). \end{aligned} \tag{23}$$

Fig. 4 illustrates our comparison between the ensemble-averaged irradiance distributions of LG beams using the OAM modes $l = +3$ propagating through underwater turbulence and the theoretical results obtained by Eq. (21). The number N of phase screens is arranged according to the turbulence conditions as $\sigma_R^2 = 0.1$ with $\mathrm{N} = 5$, $\sigma_R^2 = 0.8$ with $\mathrm{N} = 10$ and $\sigma_R^2 = 2.4$ with $\mathrm{N} = 15$. It can be seen from Fig. 4 that the numerical simulation results exhibit a good match with the analytical simulation results, except for the condition of $\sigma_R^2 = 2.4$. The differences found for $\sigma_R^2 = 2.4$ are caused by the fact that the simplified integration method and the scintillation index of Eq. (20) are only valid under weak irradiance fluctuation conditions.

C. Reference-channel Irradiance and Intermodal Crosstalk Irradiance

The underwater turbulence environment results in spreading the power of transmitted OAM mode to the adjacent OAM modes. The reference-channel irradiance is defined as the fraction of transmitted OAM mode power retained in the corresponding received mode. By contrast, the intermodal crosstalk irradiance is defined as the ratio of the power leaked from the transmitted OAM mode to the total detected power. Naturally, the reference-channel irradiance and intermodal crosstalk irradiance are fundamental quantities in evaluating the performance of OAM-based UWOC systems. We first provide the definition of the distorted wave field of a propagated LG beam associated with $p = 0$ in the presence of underwater turbulence as

$$u_{0,l,\mathrm{tur}}(\rho, \varphi, L) = (\pi)^{-1/2} u_{0,l}(\rho, \varphi, L) \exp\left[i\theta(\rho, \varphi, L)\right], \tag{24}$$

where $\theta(\rho, \varphi, L)$ represents the phase perturbation caused by single random phase screen. The coefficient representing the distorted LG beam carrying the corresponding OAM modes can be expressed as

$$a_{p,l}^m = \int_0^\infty \mathrm{d}\rho\rho \int_0^{2\pi} \mathrm{d}\varphi u_{0,l,\mathrm{tur}}(\rho, \varphi, L) u_{p,m}^*(\rho, \varphi, L). \tag{25}$$

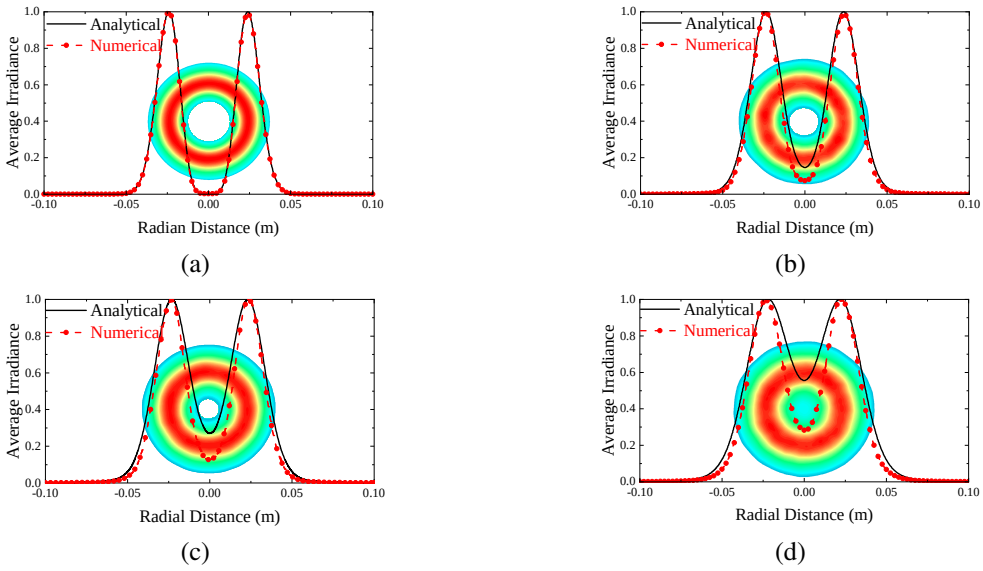

Fig. 4. Comparison between ensemble-averaged irradiance distributions of LG beams for different OAM modes $l = +3$ propagating through underwater turbulence and analytical results obtained from Eq. (26), where (a) $\sigma_R^2 = 0.1$; (b) $\sigma_R^2 = 0.8$; (c) $\sigma_R^2 = 1.2$; (d) $\sigma_R^2 = 2.4$. The distributions of intersecting surfaces normalized by the maximum value are shown from both analytical and numerical simulations.

Under the condition of $l = m$, the coefficient represents the power of transmitted OAM mode captured the receiver, otherwise, it represents the crosstalk power. In the same way, the received power of the entire detected field in the absence of turbulence can be expressed as

$$T_l = a_{0,l} = (\pi)^{-1} \int_0^{\infty} \mathrm{d}\rho\rho \int_0^{2\pi} \mathrm{d}\varphi u_{0,l}(\rho, \varphi, L) u_{0,l}^*(\rho, \varphi, L). \tag{26}$$

The instantaneous power contained in the different OAM modes at the receiver can be expressed as

$$T_l^m = \begin{cases} \sum_{p=0}^{\infty} \left|a_{p,l}^m\right|^2, & \text{if} \quad l = m \\ a_{0,l}^m, & \text{if} \quad l \neq m \end{cases}. \tag{27}$$

The distorted LG beam may spread to both the reference-mode and to the adjacent modes. In accordance with [39], for the condition of $l = m$, the transmitted power can be expressed as

$$T_l^l = (\pi)^{-1} \int_0^{\infty} \rho \mathrm{d}\rho \int_0^{2\pi} \int_0^{2\pi} u_{0,l,\mathrm{tur}}(\rho, \varphi, L) \times u_{0,l,\mathrm{tur}}^*(\rho, \varphi, L) \exp\left[-il\left(\varphi - \varphi'\right)\right] \mathrm{d}\varphi \mathrm{d}\varphi'. \tag{28}$$

Then substituting Eq. (24) into Eq. (28), T_l^l can be expressed as [16, eq. (8)]

$$T_l^l = \int_0^{\infty} r(\rho) W(\rho) \mathrm{d}\rho, \tag{29}$$

where we have:

$$r(\rho) = \rho \left| R_{0,l}^{(L)}(\rho) \right|^2, \tag{30}$$

$$W(\rho) = (\pi)^{-2} \left| \int_0^{2\pi} \mathrm{d}\varphi \exp[i\theta(\rho, \varphi, L)] \right|^2, \tag{31}$$

$$R_{0,l}^{(L)}(\rho) = \sqrt{\frac{1}{\pi(|l|)!}} \frac{2}{\omega(L)} \left[\frac{\rho\sqrt{2}}{\omega(L)}\right]^{|l|} \exp\left[\frac{-\rho^2}{\omega^2(z)}\right] \times L_0^{|l|}\left[\frac{2\rho^2}{\omega^2(L)}\right] \exp\left[\frac{-ik\rho^2 L}{2\left(L^2 + z_R^2\right)}\right] \times \exp\left[i(|l|+1)\tan^{-1}\left(\frac{L}{z_R}\right)\right]. \tag{32}$$

The term $r(\rho)$ represents the power distribution of LG beams associated with the radial distribution $p = 0$ and $W(\rho)$ denotes the weighting factor characterizing the distortion induced by underwater turbulence. Furthermore, $R_{0,l}^{(L)}(\rho)$ denotes the radial basis for the LG mode without OAM mode. With this in mind, the relationship of the reference-channel irradiance distribution and intermodal irradiance distribution can be captured by

$$P_l^m = \frac{\sum_{i=1}^N T_{l,i}^m}{\sum_{i=1}^N T_{l,i}}, \tag{33}$$

where N represents the number of phase screens, i denotes the i^{th} phane in split step Fourier transform processing. The power distribution in Eq. (32) for $i \neq 1$ can be replaced by the power of distorted beam.

III. GGD Fitting Tests Compared with Simulations

Before proceeding further, we provide a diagram depicted in Fig. 5, which visualizes the logical flow of our analysis of this paper for the readers to assiste them in relating the parameters of the GGD model to the system parameters of the OAM-UWOC model.

A. Generalized Gamma Distribution Using An Additional Independent Parameter

In [17], the GGD having three parameters was used for modelling the irradiance fluctuations of OAM-based Free Space Optical (FSO) multiplexing systems. By contrast, here

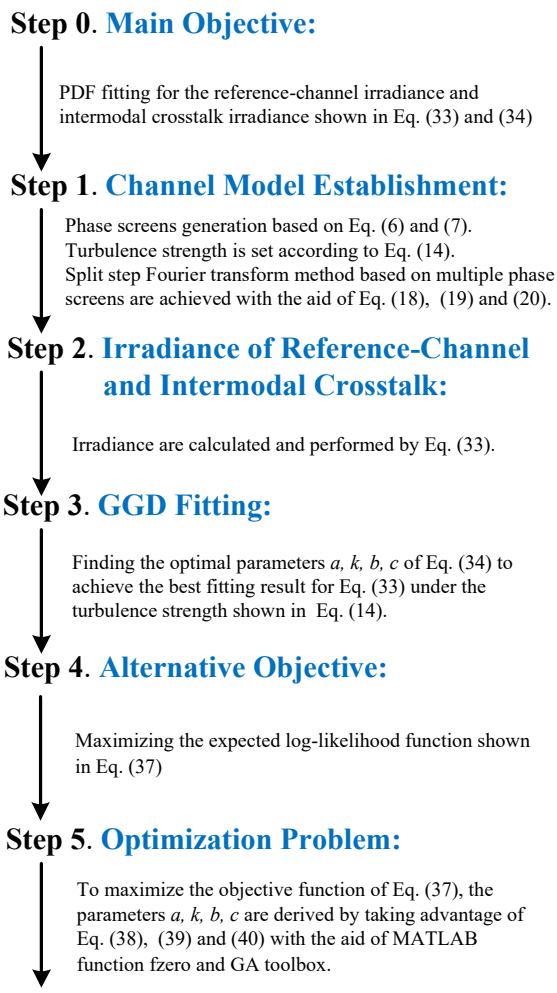

Fig. 5. Flow of the mathematical analysis.

the GGD model having an additional independent parameter is proposed for flexible curve fitting, The corresponding expression can be formulated as

$$f_I(I;a,k,b,c) = cb\frac{I^{bk-1}}{a^{bk}}\frac{\exp\left(-(I/a)^b\right)}{\Gamma(k)}, \tag{34}$$

where I denotes the irradiance fluctuations of the received optical power in the face of underwater turbulence. The variance a and b represent the combined shape parameters and c denotes the independent amplitude control parameter, while k is the scaling parameter of the GGD and $\Gamma(\cdot)$ is the Gamma function. In particular, for $b = 1$, the GGD becomes the conventional Gamma distribution (GD) and when $a = b = 1$, the GGD distribution degenerates to the Exponential distribution (ED).

The nth moment of I defined as $\mathbb{E}[I^n] \triangleq \int_0^\infty I^n f_I(I)dI$ can be deduced by substituting Eq. (34) into the equation mentioned above and the resultant expression can be written as [40, eqs. (3.351/3) and (3.478/1)]

$$\mathbb{E}[I^n] = ca^n\frac{\Gamma\left(k+\frac{n}{b}\right)}{\Gamma(k)}, \tag{35}$$

where $\mathbb{E}$ represents the expected value.

B. MLE for The Parameters of The GGD Model

The challenge in estimating and computing the parameters of the GGD model is that no explicit expressions are available for the shape parameter estimators. In this paper, the MLE method of [21] is applied for the parameter estimation in GGD. To find the maximum likelihood solution of matching the GGD model, the expectation maximum iteration algorithm (EMA) and genetic algorithms (GA) are adopted. Both the EMA and the GA are iterative search procedures suitable for finding the globalby optimal solutions. To construct and solve the associated equations, random irradiance measurements $P_{l,i}^m$ associated with a hidden unobserved binary variable $z_i = 1$ are needed [21].

The E-step of the EMA relies on computing the expected values of the hidden variables z_i, given the incomplete or observed data set $\{P_{l,i}^m\}_{i=1}^N$ and then calculating the expected log-likelihood function. Based on Bayes' law, these quantities are represented as

$$\gamma_i \triangleq \mathbb{P}\left[z_i = 1 \mid \{P_{l,i}^m\}_{i=1}^N\right] = \frac{1}{f(P_{l,i}^m;a,k,b,c)}. \tag{36}$$

The ensuing M-step maximizes the expected log-likelihood with respect to the parameters, where the log-likelihood function can be expressed as [41]

$$\begin{aligned} L\left(P_{l,i}^m;a,k,b,c\right) &= \gamma_i \log\left(c/\left(b^{bk}\Gamma(k)\right)\right) \\ &+ (bk-1)\sum_{i=1}^N \gamma_i \log(P_{l,i}^m) - a^{-b}\sum_{i=1}^N \gamma_i (P_{l,i}^m)^b. \end{aligned} \tag{37}$$

To maximize the objective function of Eq. (37) over the variables a, k, b and c, the MLE should satisfy the following set of equations with γ_i [42]

$$k = \frac{b^{-1}\sum_{i=1}^N \gamma_i}{\frac{\sum_{i=1}^N \log\gamma_i \sum_{i=1}^N \gamma_i \left(P_{l,i}^m\right)^b \log(P_{l,i}^m)}{\sum_{i=1}^N \gamma_i (P_{l,i}^m)^b} - \sum_{i=1}^N \gamma_i \log(P_{l,i}^m)}, \tag{38}$$

$$a^b = \frac{\sum_{i=1}^N \gamma_i (P_{l,i}^m)^b}{\sum_{i=1}^N \gamma_i k}, \tag{39}$$

$$b\sum_{i=1}^N \gamma_i \log(P_{l,i}^m) - \sum_{i=1}^N \log(a^b) - \sum_{i=1}^N \gamma_i \psi_0(k) = 0, \tag{40}$$

where $\psi_0(\cdot)$ denotes the digamma function. By using the MATLAB function fzero, the parameter b can be derived by substituting Eq. (36), Eq. (38) and Eq. (39) into Eq. (40). The parameters a and k can be retrieved, provided that b is obtained. With the aid of the GA from the MATLAB global optimization toolbox, the parameter c can be obtained based on a, k and b.

To evaluate the GGD model for different OAM modes in different underwater turbulence environments, the transmission conditions are set as follows. The Monte-Carlo simulations characterizing the propagation of LG beams through underwater turbulence are performed at the wavelength of $\lambda = 512\text{nm}$. The propagation distance is equal to $z = 50\text{m}$ and the beam waist in the transmit plane is $w_0 = 2.8\text{cm}$. The microscale of underwater turbulence is set to $\eta = 0.1\text{mm}$ and the number

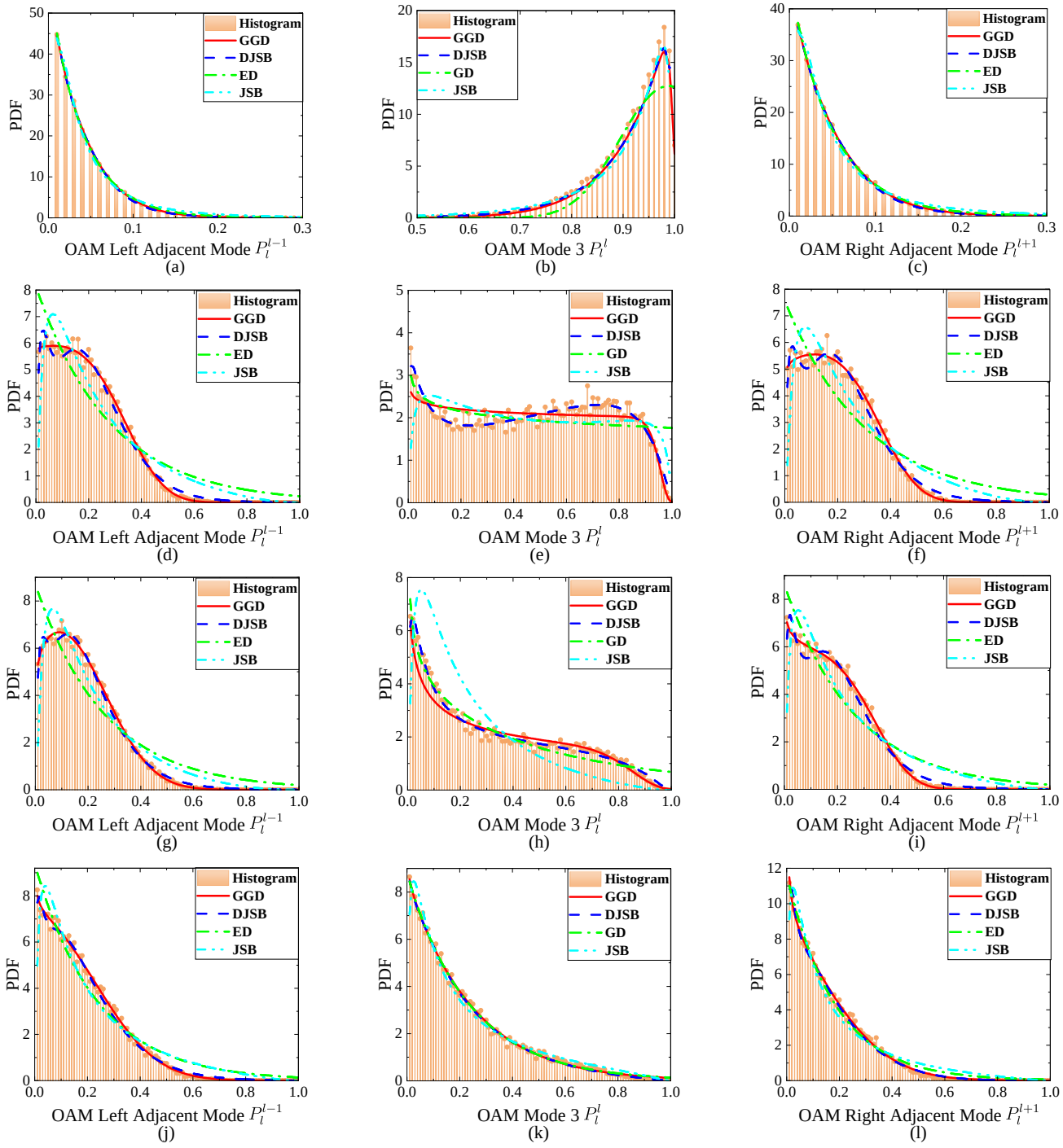

Fig. 6. Histograms of the reference-channel and adjacent channel crosstalk irradiance samples generated by Monte-Carlo simulations for OAM **mode 3**. The measured data are depicted with fitted PDFs via the GGD, the DJSB, the GD, the ED and the JSB under various levels of turbulence for (a), (b), (c) $\sigma_R^2 = 0.1$; (d), (e), (f) $\sigma_R^2 = 0.8$; (g), (h), (i) $\sigma_R^2 = 1.2$; (j), (k), (l) $\sigma_R^2 = 2.4$.

of grid points for each phase screen, transmitting plane and receiving plane are set as 1024×1024 pixels. The transmitted OAM mode set is $\mathcal{L} = \{+1, +3, +5, +7\}$ and the number N of phase screens are arranged in-line with the turbulence strength as $\sigma_R^2 = 0.1$ with $\mathrm{N} = 5$, $\sigma_R^2 = 0.8$ with $\mathrm{N} = 10$ and $\sigma_R^2 = 2.4$ with $\mathrm{N} = 15$. We measured 50,000 samples for the reference-channel and intermodal crosstalk irradiance fluctuations for the parameter extraction under a classic IM/DD setup.

The goodness of fitting test is shown by making comparisons between the target histograms of irradiance generated according to Monte-Carlo simulations and the corresponding PDF deduced from the analytical distributions. Moreover, the performance superiority of the GGD model will be shown by comparing it to the dual Johnson S_B (DJSB) distribution, Gamma distribution (GD), Johnson S_B distribution (JSB) and Exponential distribution (ED) under different channel conditions. It is worth accentuating that the EMA can be used for the estimation of the GD and ED. The parameters of JSB and

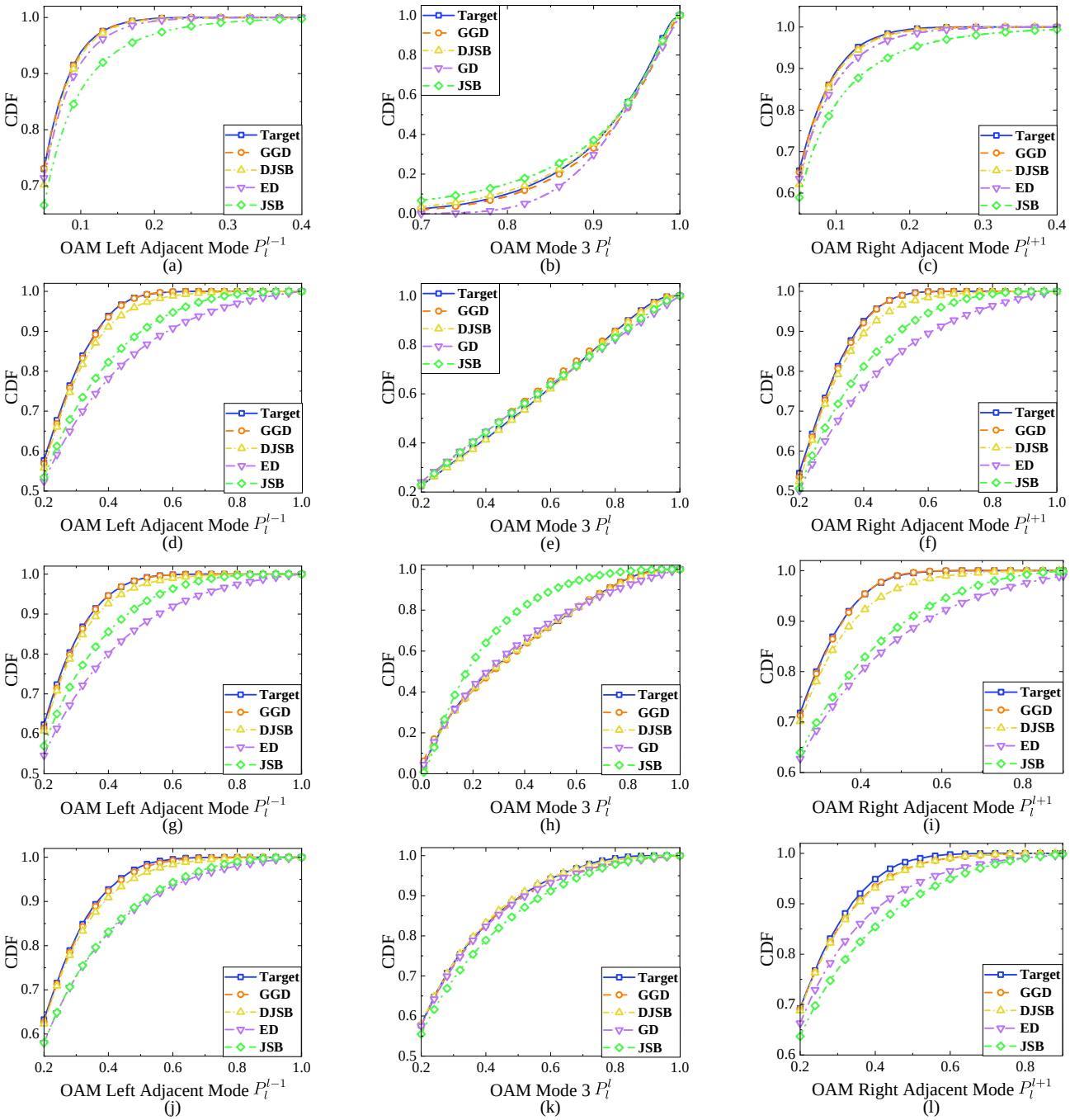

Fig. 7. Empirical CDFs of the reference-channel and adjacent channel crosstalk irradiance calculated according to histogram samples generated by Monte-Carlo simulations for OAM **mode 3**. The calculated empirical data are depicted with analytical CDFs via the GGD, the DJSB, the GD, the ED and the JSB under various levels of turbulence for (a), (b), (c) $\sigma_R^2 = 0.1$; (d), (e), (f) $\sigma_R^2 = 0.8$; (g), (h), (i) $\sigma_R^2 = 1.2$; (j), (k), (l) $\sigma_R^2 = 2.4$.

DJSB can be retrieved according to [15], [16]. To validate the goodness of fit for the GGD models, the statistical calculations of the CDF are also derived as $F(x) = \int_{-\infty}^{x} f_I(I,\theta)dI$ for different OAM modes and the goodness of fit is quantified in terms of the RMSE defined as

$$\text{RMSE} = \sqrt{\frac{1}{N}\sum_{k=1}^{N}\left(\hat{F}^k(P_{l,i}^m) - F^k(P_{l,i}^m)\right)^2}, \tag{41}$$

where $\hat{F}^k(\cdot)$ denotes the empirical distribution function and $F^k(\cdot)$ represents the theoretical CDF. For the sake of comparison, the PDF and CDF distribution expressions of the different statistical models are listed in Table II at a glance. The function $\Psi(\cdot)$ represents the cumulative distribution function of a standard normal distribution, while Meijer's G function is available in MATLAB.

In Fig. 6, the MLE-based fitting of different statistical distribution models are portrayed both for the reference mode and for the adjacent crosstalk irradiance mode. The distributions of the transmitted OAM of mode $l = +3$ is chosen from $l \in \mathcal{L} = \{+1, +3, +5, +7\}$ as an example and at the receiver $m \in \mathcal{M} = \{l-1, l, l+1\}$ are regarded as the left adjacent

TABLE II
PDF AND CDF OF STATISTICAL DISTRIBUTION MODELS

Statistical Distribution	**Distribution of PDF f_I**	**Distribution of CDF F_I**
Generalized Gamma [43]	$\frac{cb}{I\Gamma(k)}\mathrm{G}_{0,1}^{1,0}\left[\left(\frac{I}{a}\right)^b \middle\vert \begin{matrix} - \\ k \end{matrix}\right]$	$\frac{c}{\Gamma(k)}\mathrm{G}_{1,1}^{1,2}\left[\left(\frac{I}{a}\right)^b \middle\vert \begin{matrix} 1 \\ k,0 \end{matrix}\right]$
Gamma [44]	$\frac{c}{I\Gamma(k)}\mathrm{G}_{0,1}^{1,0}\left[\left(\frac{I}{a}\right) \middle\vert \begin{matrix} - \\ k \end{matrix}\right]$	$\frac{c}{\Gamma(k)}\mathrm{G}_{1,1}^{1,2}\left[\left(\frac{I}{a}\right) \middle\vert \begin{matrix} 1 \\ k,0 \end{matrix}\right]$
Exponential [45]	$\frac{c}{I\Gamma(k)}\mathrm{G}_{0,1}^{1,0}\left[I \middle\vert \begin{matrix} - \\ k \end{matrix}\right]$	$\frac{c}{\Gamma(k)}\mathrm{G}_{1,1}^{1,2}\left[I \middle\vert \begin{matrix} 1 \\ k,0 \end{matrix}\right]$
Johnson S_B [46]	$\frac{\tau}{\sqrt{2\pi}}\frac{s}{I(1-I)}\exp\left\{-\frac{1}{2}\left[\vartheta+\tau\ln\left(\frac{I}{1-I}\right)\right]^2\right\}$	$\Psi\left[\vartheta+\tau\log\left(\frac{I}{1-I}\right)\right]$
Dual Johnson S_B [16]	$\frac{1}{2}\left[\frac{\tau_1}{\sqrt{2\pi}I(1-I)}\exp\left\{-\frac{1}{2}\left[\vartheta_1+\tau_1\ln\left(\frac{I}{1-I}\right)\right]^2\right\}\right.$ $\left.+\frac{\tau_2}{\sqrt{2\pi}I(1-I)}\exp\left\{-\frac{1}{2}\left[\vartheta_2+\tau_2\ln\left(\frac{I}{1-I}\right)\right]^2\right\}\right]$	$\frac{1}{2}\Psi\left[\vartheta_1+\tau_1\log\left(\frac{I}{1-I}\right)\right]$ $+\frac{1}{2}\Psi\left[\vartheta_2+\tau_2\log\left(\frac{I}{1-I}\right)\right]$

TABLE III
RMSE AND ESTIMATED PARAMETERS OF THE GGD, GD, JSB, AND DJSB DISTRIBUTION WITH TARGET EMPIRICAL CDF FOR THE SELF-CHANNEL MEASURED FLUCTUATING IRRADIANCE IN $\sigma_R^2 = 0.8$

OAM Mode	**Statistical Distribution Model**							
	Generalized Gamma		**Gamma**		**Johnson** S_B		**Dual Johnson** S_B	
	$\{a,k,b,c\}$	RMSE	$\{a,k,c\}$	RMSE	$\{\vartheta,\tau,s\}$	RMSE	$\{\vartheta_1,\tau_1,\vartheta_2,\tau_2\}$	RMSE
1	0.061 0.977 49.387 1.966	$2.82\mathrm{E}-03$	9.287 0.103 3.069	$6.36\mathrm{E}-02$	1.036 -0.872 -1.979	$4.36\mathrm{E}-03$	-1.33 0.983 -0.736 0.768	$3.60\mathrm{E}-03$
3	0.029 0.958 36.559 2.014	$8.82\mathrm{E}-03$	0.892 31.046 41.92	$1.04\mathrm{E}-02$	-0.106 -0.61 -1.988	$9.36\mathrm{E}-03$	-0.454 0.928 0.53 0.541	$3.44\mathrm{E}-03$
5	0.029 0.937 25.643 2.045	$4.30\mathrm{E}-03$	0.789 1.915 3.926	$5.10\mathrm{E}-02$	0.366 0.564 1.99	$7.14\mathrm{E}-02$	1.047 0.626 -0.286 0.883	$4.92\mathrm{E}-03$
7	0.061 0.881 10.355 2.107	$4.80\mathrm{E}-03$	0.793 0.699 2.486	$7.01\mathrm{E}-02$	1.245 0.809 2.114	$6.24\mathrm{E}-00$	0.051 0.858 1.486 0.705	$4.67\mathrm{E}-03$

and right adjacent crosstalk modes in three different underwater turbulence conditions. For each distribution, a GGD model fitting along with DJSB, JSB, GD or ED model are plotted. The transmitted OAM mode of $l = +3$ and the turbulence intensity are set as $\sigma_R^2 = 0.1$ for the first row, $\sigma_R^2 = 0.8$ for the second row, $\sigma_R^2 = 1.2$ for the third row and $\sigma_R^2 = 2.4$ for the fourth row, respectively. The center column corresponds to the reference-channel irradiance distribution associated with $l = m$. The left column and right column portray the best fitting distributions for the adjacent crosstalk OAM modes. It can be observed from Fig. 6 that the GGD model generally has quite an accurate fit with the histograms of the simulated samples of the various turbulence conditions, except for the reference-channel irradiance distribution at $\sigma_R^2 = 0.8$. The GGD model agrees with the histograms of the Monte-Carlo simulated samples better than the GD, ED and JSB model. Indeed, it is seen that the GGD yields a potentially even better fit to the measured data than the DJSB, except for the reference-channel irradiance distribution at $\sigma_R^2 = 0.8$.

Fig. 7 compares the empirical and analytical CDFs of different statistical models of the OAM mode of $l = +3$. The empirical CDFs of the reference-channel and adjacent crosstalk irradiance are calculated based on the samples generated via Monte-Carlo simulations. The analytical CDFs of the different statistical models are plotted along with the empirical CDFs under various turbulence conditions. The turbulence environment is determined by $\sigma_R^2 = 0.1$ for the first row, $\sigma_R^2 = 0.8$ for the second row, $\sigma_R^2 = 1.2$ for the third row and $\sigma_R^2 = 2.4$ for the fourth row, respectively. The center column shows the reference-channel irradiance distribution, while the

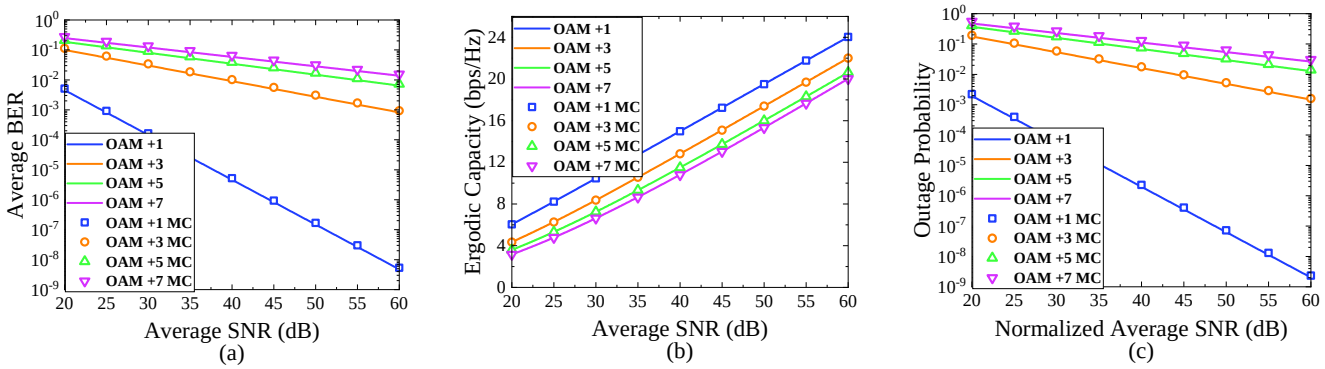

Fig. 8. (a) Average BER vs average SNR from Eq. (50). (b) Ergodic capacity vs average SNR from Eq. (47). (c) Outage probability vs normalized average SNR from Eq. (48). The transmitted LG beam is single OAM mode from $\mathcal{L} = \{+1, +3, +5, +7\}$ and the turbulence level is set as $\sigma_R^2 = 0.8$.

left and right columns show the adjacent crosstalk irradiance CDFs. It can be seen from Fig. 7 that the turbulence does have a distinctive impact on the CDFs. To elaborate on Fig. 7, the CDFs of the reference-channel mode are slightly shifted to the right, while the adjacent crosstalk modes are somewhat shifted to the left and tend to saturate more rapidly, when the underwater turbulence is weak. In addition, one can see from Fig. 7 that as the turbulence levels are increased from $\sigma_R^2 = 0.8$ to $\sigma_R^2 = 2.4$, we observe no substantial changes in the CDFs of crosstalk irradiance distribution upon varying l. However, changing the turbulence levels obviously affects of CDFs of the reference-channel irradiance.

For the sake of comparison, the RMSE of CDFs of the reference-channel modes $l \in \mathcal{L} = \{+1, +3, +5, +7\}$ associated with different statistical distributions and $\sigma_R^2 = 0.8$ are given and the estimated parameters of the statistical distributions are listed in the Table III. Observe from Table III that both the GGD model and DJSB model provide better fit in conjunction with a RMSE less than 1×10^{-2} distributions compared to the Gamma and Jonson S_B.

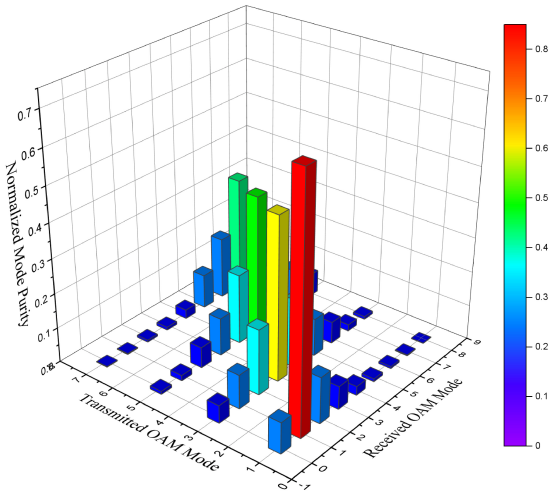

Fig. 9. The average normalized mode purity for P_l^l and P_l^m for $l \in \mathcal{L} = \{+1, +3, +5, +7\}$ calculated for 50,000 samples. The turbulence level is set to $\sigma_R^2 = 0.8$.

IV. PERFORMANCE ANALYSIS

In this section, the performance analysis of both a single OAM mode beam and of multiple OAM mode beams are provided for an IM/DD on-off keying (OOK) modulated UWOC system. The underwater turbulence is set to $\sigma_R^2 = 0.8$ for ensuring that the Monte-Carlo simulations are consistent with the analytical results and the underwater turbulence has a significant impact on the channel characteristics. We consider scenarios in which the effects of scattering, absorption and inter symbol interference (ISI) do not significantly degrade the performance of the system. The PDF and CDF expressions derived in Table II can be used for simplifying the calculation of the performance metrics, such as the average BER, the ergodic capacity and the outage probability. The correctness of the mathematical formulae is verified by means of Monte-Carlo simulations.

Assuming that the LG beams propagating through underwater turbulence channels and contaminated by additive white Gaussian noise (AWGN) in IM/DD systems, where both the photoelectric conversion efficiency of the signal and the detector's thermal noise are also taken into account. The signal at the receiver can be expressed as

$$y = \eta I x + n, \tag{42}$$

where η represents the photoelectric conversion efficiency, I denotes the received signal irradiance, $x \in \{0, 1\}$ denotes the information bits, while n is the AWGN having zero mean and a variance of $N_0/2$. The instantaneous electrical signal-to-noise ratio (SNR) is defined as $\gamma \triangleq \eta^2 I^2 / N_0$ and the average electrical SNR can be expressed as $\mu \triangleq \eta^2 \mathbb{E}[I]^2 / N_0$, which is related to the average SNR defined as $\bar{\gamma} \triangleq \left(\mu \mathbb{E}[I^2]\right) / \mathbb{E}[I]^2$. By using Eq. (35), the average electrical SNR μ can be expressed as

$$\mu = \frac{\bar{\gamma}}{a^2 c \Gamma(k + 2/b)/\Gamma(k)}. \tag{43}$$

Upon employing [47, eqs. (2.9.4), (2.1.4), and (2.1.9)], Eq. (34) can be written as

$$f_\gamma(\gamma; a, k, b, c) = \frac{cb}{2\gamma\Gamma(k)} \mathrm{G}_{0,1}^{1,0}\left[\left(\frac{\gamma}{a^2\mu}\right)^{b/2} \middle| \begin{matrix} - \\ k \end{matrix}\right]. \tag{44}$$

By using the definition of Meijer's G function in [47, eq.

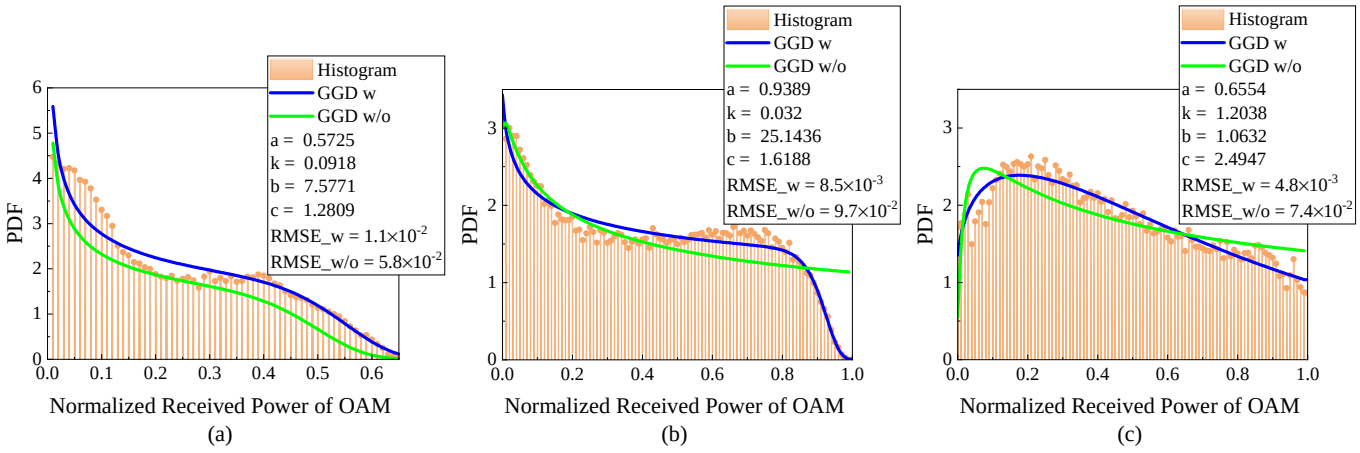

Fig. 10. Histograms of the the reference-channel irradiance from $|\mathcal{M}| = 4$ MIMO OAM-FSO system based on MRC technique with same transmitted data for (a) $l = \{+1, +3\}$; (b) $l = \{+1, +3, +5\}$; (c) $l = \{+1, +3, +5, +7\}$. The measured data are depicted with fitted PDFs via the GGD distribution with/witout additional independent parameter under turbulence intensity $\sigma_R^2 = 0.8$.

(2.9.1)], the CDF of γ expressed as $F(\gamma) = \int_{-\infty}^{\gamma} f_\gamma(\gamma)d\gamma$ can be obtained as

$$F_\gamma(\gamma; a, k, b, c) = \frac{c}{\Gamma(k)} \mathrm{G}_{1,2}^{1,1}\left[\left(\frac{\gamma}{a^2\mu}\right)^{b/2} \middle| \begin{matrix} 1 \\ k, 0 \end{matrix}\right]. \quad (45)$$

A. Ergodic Capacity

The ergodic capacity is defined as [48, eq. (26)]

$$\mathrm{C}_{erg} \triangleq \mathbb{E}\left[\ln\left(1 + \frac{e}{2\pi}\gamma\right)\right]. \quad (46)$$

By substituting Eq. (44) into Eq. (46), the ergodic capacity of the single OAM mode based UWOC system can be expressed in closed-form by using [47, eq. (2.9.1)], [21, eq. (31)]

$$\begin{aligned}\mathrm{C}_{erg} &= \int_0^\infty \ln\left(1 + \frac{e}{2\pi}\gamma\right) f_\gamma(\gamma)d\gamma \\ &= \frac{c}{\Gamma(k)} \mathrm{H}_{2,3}^{3,1}\left[\left(\frac{2\pi}{a^2 e\mu}\right)^{b/2} \middle| \begin{matrix} (0, b/2)(1, 1) \\ (k, 1)(0, 1)(0, b/2) \end{matrix}\right].\end{aligned} \quad (47)$$

Fox's H function can be evaluated using MATHEMATICA

B. Outage Probability

Another important performance metric of interest is the outage probability defined as the likelihood of the instantaneous SNR falling below the threshold γ_{th}. The outage probability P_{out} of the UWOC system single OAM mode based can be expressed according to Eq. (45) as

$$\mathrm{P}_{\text{out}} = \Pr\left(\gamma < \gamma_{th}\right) = F_\gamma\left(\gamma_{th}\right). \quad (48)$$

C. Average BER

A unified expression for the average BER of SISO IM/DD systems using OOK modulation scheme can be expressed as [49]

$$\mathrm{P}_e = \frac{\delta}{2\Gamma\left(p_k\right)} \sum_{k=1}^{n} \int_0^\infty \Gamma\left(p_k, q_k\gamma\right) f_\gamma(\gamma)d\gamma, \quad (49)$$

where $n = 1$, $\delta = 1$, $p_k = 1/2$, $q_k = 1/4$ depend on the OOK modulation format and on the specific IM/DD detection technique [21]. The variable $\Gamma(\cdot, \cdot)$ represents the upper incomplete Gamma function defined as $\Gamma(p, x) = \int_x^\infty u^{p-1}e^{-u}du$. Upon substituting Eq. (44) into Eq. (49) and by utilizing [47, eq(2.9.1)], [50, eq.(3.381/4)] and [51, eq.(1.1)], the average BER expression of OOK modulation may be expressed using Fox's function as

$$\mathrm{P}_e = \frac{c}{4\Gamma(k)} \mathrm{H}_{2,2}^{1,2}\left[\left(\frac{4}{a^2\mu}\right)^{b/2} \middle| \begin{matrix} (1, 1)\left(\frac{1}{2}, \frac{b}{2}\right) \\ (k, 1)(0, 1) \end{matrix}\right]. \quad (50)$$

D. SISO IM/DD OOK System

In this section, numerical results of the average BER, the ergodic capacity and the outage probability of OAM-based SISO UWOC systems having $l \in \mathcal{L} = \{+1, +3, +5, +7\}$ is investigated. The turbulence level is set to $\sigma_R^2 = 0.8$ and the parameters of the GGD model are listed in Table III. The above mentioned performance metrics are compared to the result of our Monte-Carlo simulations in Fig. 8.

In Fig. 8(a), the average BER of the IM/DD receiver is presented as a function of the average SNR μ. As expected, the BER decreases as the SNR increases and the BER performance degrades as the number of OAM modes increases. Observe from the figure that the best BER performance is attained by $l = +1$, which performs much better than the other OAM modes. In Fig. 8(b), the ergodic capacity associated with different OAM modes is compared. Similar to the results of Fig. 8(a), the best capacity is achieved by the OAM mode $l = +1$. The only difference is that its gain over other modes is not as high as in Fig. 8(a). The outage probability of different OAM modes as a function of the normalized average SNR is shown in Fig. 8(c). It can be observed that the OAM mode $l = +1$ has a huge advantage over the other three OAM modes. Finally, the results obtained from the analytical expressions agree well with those of the Monte-Carlo simulations.

E. MIMO IM/DD OOK System

In this section, we consider a OOK IM/DD OAM-based UWOC system equipped with $l \in \mathcal{L} = \{+1, +3, +5, +7\}$

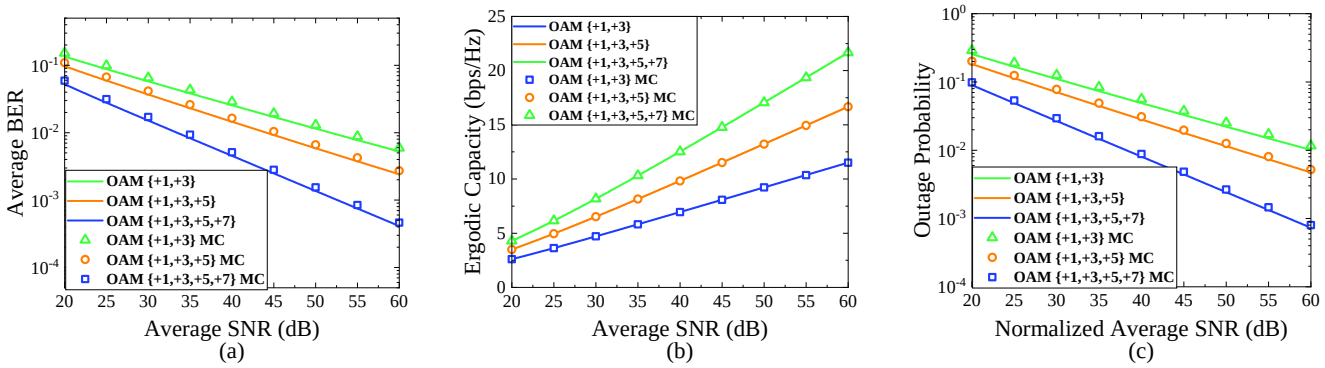

Fig. 11. The performance metrics of MIMO OAM UWOC system based on MRC technique with same transmitted data. The transmitted OAM modes are $l \in \mathcal{L} = \{+1, +3, +5, +7\}$ and the turbulence level is set as $\sigma_R^2 = 0.8$. (a) Average BER vs average SNR. (b) Ergodic capacity vs average SNR. (c) Outage probability vs normalized average SNR.

transmit apertures and $\mathcal{M}$ receive apertures. In the absence of channel state information, mode selection and space-time coding, relying on spatial diversity combining is applied to the MIMO OAM-based UWOC system, when the same data is transmitted and different data is transmitted by the different modes, respectively.

It should be noted that when a LG beam propagates through underwater turbulence, the power of the reference-channel mode will spread into other modes, thus causing crosstalk between the different OAM modes and degrading the performance of MIMO systems. The average normalized mode purity of the reference-channel and intermodal crosstalk can be calculated from Eq. (33) with the aid of Monte-Carlo samples. In Fig. 9, the normalized mode purity is presented for $l \in \mathcal{L} = \{+1, +3, +5, +7\}$ and $\sigma_R^2 = 0.8$. As clearly seen from this figure, the power in the transmitted OAM mode is much higher than the power spread into other modes. Additionally, the power contained in $l = +1$ is much higher than that in other modes.

Based on the classic spatial diversity technique, a MIMO system having multiple OAM beams for $\mathcal{L} = \mathcal{M} \in \{+1, +3, +5, +7\}$ is considered. The electrical SNR at the receiver using the MRC technique for the same transmitted data for all modes can be expressed as:

$$\gamma_m = \frac{\eta^2}{M^2 N_0} \sum_{m \in \mathcal{M}} w_m \left(\sum_{l \in \mathcal{L}} P_l^m \right)^2, \tag{51}$$

where η denotes the photodetector's quantum efficiency and $M = size(\mathcal{M})$ represents numbers of channels regarded as the average coefficient for convenient comparison of SISO and MIMO scenarios. The coefficient w_m denotes the weighting coefficients of the different channels and the default setting is 1, unless otherwise specified [17]. The exact PDF of our MIMO system involves the sum of the reference-channel and intermodal crosstalk imposed by the other independent transmitted channels. The quantity $P_{\mathcal{L}} = \frac{1}{M} \sqrt{\sum_{m \in \mathcal{M}} w_m \left(\sum_{l \in \mathcal{L}} P_l^m \right)^2}$ can be considered as the PDF of our MIMO system, which can be estimated by the GGD distribution, while the average electrical SNR can be described as $\gamma_m \triangleq \eta^2 {P_{\mathcal{L}}}^2 / N_0$. The BER performance, ergodic capacity and outage probability can be deduced directly with the aid of Eqs. (47), (48) and (50). In Fig. 10, the PDF of our MIMO system associated with $l = \{+1, +3\}$, $l = \{+1, +3, +5\}$ and $l = \{+1, +3, +5, +7\}$ is represented by the GGD distribution model associated both with and without additional independent parameters, respectively. Observe from Fig. 10, that the GGD model associated with extra parameter outperforms the one proposed in [17].

In Fig. 11, the performance metrics of our OAM-based MIMO UWOC system employing spatial diversity reception and the same transmitted signal in all modes are presented under the turbulence condition of $\sigma_R^2 = 0.8$. Observe from the figure that the set $\mathcal{M} = \{+1, +3, +5, +7\}$ has the lowest BER as well as outage probability and the highest capacity. This is not unexpected, because the other OAM modes spread onto the transmitted mode have a positive influence on the performance metrics of system when the same signal is transmitted over all the different channels. Finally, the Monte-Carlo simulations exhibit an excellent match with the numerical results.

In the previous discussions, the performance metrics of multiple OAM beams based on MRC spatial diversity reception using the same transmitted data for all modes were investigated and presented. However, when the transmitted data are different in each mode of all OAM beams, the power spread into the reference-channel from the other transmitted modes should be considered as signal-dependent noise [32]. For this reason, the performance metrics of our MIMO system using different transmitted data are investigated next based on the GGD model. In this channel, each constituent channel is modeled as a binary-symmetric channel (BSC). Each crosstalk signal component spread from the other transmitted OAM modes is regarded as an independent Gaussian source and the average electrical SNR μ_m can be expressed as

$$\mu_m = \frac{\eta^2}{M^2} \sum_{m \in \mathcal{M}} w_m \left(P_m^m\right)^2 \left(\eta^2 \left(\sum_{l \in \mathcal{L}}^{l \neq m} P_l^m \right)^2 + N_0 \right)^{-1}, \tag{52}$$

where the term μ_m has been conveniently represented by the mode purity of the reference-channel and by the intermodal crosstalk, while $N_0 / \left(P_m^m\right)^2$ can be viewed as the reciprocal of the average SNR associated with $1/\bar{\gamma}$. The PDF of our SISO system can be directly harnessed for deriving that of

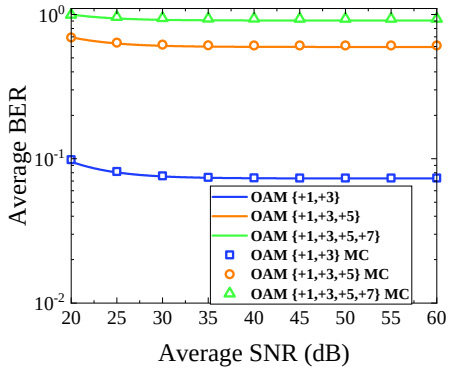

Fig. 12. The Ergodic capacity vs average SNR of MIMO OAM UWOC system with different transmitted data. The transmitted OAM modes are $l \in \mathcal{L} = \{+1, +3, +5, +7\}$ and the turbulence level is set as $\sigma_R^2 = 0.8$.

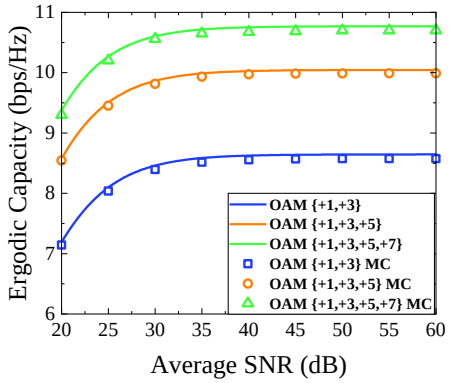

Fig. 13. The Average BER vs average SNR of MIMO OAM UWOC system with different transmitted data. The transmitted OAM modes are $l \in \mathcal{L} = \{+1, +3, +5, +7\}$ and the turbulence level is set as $\sigma_R^2 = 0.8$.

the multiplexing system, in which the crosstalk imposed by the independent channels degrades the performance of our MIMO system. The average BER and the ergodic capacity can be derived by relying on Eq. (47) and Eq. (50), respectively.

In Figs. 12 and 13, the ergodic capacity and the average BER are depicted as a function of average SNR for our OAM-based MIMO system having multiple OAM beams carrying different transmitted data in each mode at the turbulence level of $\sigma_R^2 = 0.8$. As expected, the capacity increases and the BER decreases as the SNR increases, but the curves tend to converge when the SNR reaches 35dB. Although the set $l = \{+1, +3, +5, +7\}$ achieves better capacity than $l = \{+1, +3, +5\}$ and $l = \{+1, +3\}$, the BER trend is reversed due to the contamination spread from the other transmitted OAM modes. In a nutshell, the BER performance degrades as the number of modes increases owing to the crosstalk.

V. Conclusion

Underwater turbulence channels based on multiple phase screens have been investigated. The GGD model having an additional independent parameter was employed for characterizing OAM UWOC systems and the performance metrics of both SISO and MIMO systems were analyzed. The Monte-Carlo simulations closely matched the analytical results for moderate turbulence intensity. Compared to the DJSB, GD, JSB and ED model, the GGD model yields at least as good, or even better matches for diverse turbulence conditions. The closed-form expressions of average BER, ergodic capacity and outage probability were quantified for single OAM mode based UWOC transmission systems. The spatial diversity gains based on MRC reception and multiple OAM beams conveying the same data over the different modes were also quantified. Significant performance improvements were achieved. However, when transmitting different data over the different attained modes, the crosstalk degraded the system performance.

References

[1] M. Jahanbakht, W. Xiang, L. Hanzo, and M. R. Azghadi, "Internet of underwater things and big marine data analytics—a comprehensive survey," *IEEE Communications Surveys Tutorials*, pp. 1–1, Jan. 2021.

[2] H. Guo, Z. Sun, and P. Wang, "Joint design of communication, wireless energy transfer, and control for swarm autonomous underwater vehicles," *IEEE Transactions on Vehicular Technology*, vol. 70, no. 2, pp. 1821–1835, Jan. 2021.

[3] M. V. Jamali, P. Nabavi, and J. A. Salehi, "MIMO underwater visible light communications: Comprehensive channel study, performance analysis, and multiple-symbol detection," *IEEE Transactions on Vehicular Technology*, vol. 67, no. 9, pp. 8223–8237, May 2018.

[4] J. Wang, J. Yang, I. M. Fazal, N. Ahmed, Y. Yan, H. Huang, Y. Ren, Y. Yue, S. Dolinar, M. Tur, and A. E. Willner, "Terabit free-space data transmission employing orbital angular momentum multiplexing," *Nature Photonics*, vol. 6, no. 7, pp. 488–496, Jul. 2012.

[5] A. E. Willner, H. Huang, Y. Yan, Y. Ren, N. Ahmed, G. Xie, C. Bao, L. Li, Y. Cao, Z. Zhao, J. Wang, M. P. J. Lavery, M. Tur, S. Ramachandran, A. F. Molisch, N. Ashrafi, and S. Ashrafi, "Optical communications using orbital angular momentum beams," *Advances in Optics and Photonics*, vol. 7, no. 1, pp. 66–106, Mar. 2015.

[6] Y. Zhao, A. Wang, L. Zhu, W. Lv, J. Xu, S. Li, and J. Wang, "Performance evaluation of underwater optical communications using spatial modes subjected to bubbles and obstructions," *Optics Letters*, vol. 42, no. 22, pp. 4699–4702, Nov. 2017.

[7] M. V. Jamali, A. Mirani, A. Parsay, B. Abolhassani, P. Nabavi, A. Chizari, P. Khorramshahi, S. Abdollahramezani, and J. A. Salehi, "Statistical studies of fading in underwater wireless optical channels in the presence of air bubble, temperature, and salinity random variations," *IEEE Transactions on Communications*, vol. 66, no. 10, pp. 4706–4723, May 2018.

[8] X. Yi, Z. Li, and Z. Liu, "Underwater optical communication performance for laser beam propagation through weak oceanic turbulence," *Applied Optics*, vol. 54, no. 6, pp. 1273–1278, Feb. 2015.

[9] B. L. McGlamery, "Restoration of turbulence-degraded images*," *Journal of The Optical Society of America A*, vol. 57, no. 3, pp. 293–297, Mar. 1967.

[10] M. C. Roggemann, B. M. Welsh, D. Montera, and T. A. Rhoadarmer, "Method for simulating atmospheric turbulence phase effects for multiple time slices and anisoplanatic conditions," *Applied Optics*, vol. 34, no. 20, pp. 4037–4051, Jul. 1995.

[11] J. Schmidt, "Numerical simulation of optical wave propagation with examples in MATLAB." Society of Photo-Optical Instrumentation Engineers, 2010.

[12] W. Wang, P. Wang, L. Guo, W. Pang, W. Chen, A. Li, and M. Han, "Performance investigation of OAMSK modulated wireless optical system over turbulent ocean using convolutional neural networks," *Journal of Lightwave Technology*, vol. 38, no. 7, pp. 1753–1765, Apr. 2019.

[13] S. Li, L. Yang, D. B. da Costa, J. Zhang, and M. S. Alouini, "Performance analysis of mixed RF-UWOC dual-hop transmission systems," *IEEE Transactions on Vehicular Technology*, vol. 69, no. 11, pp. 14 043–14 048, Oct. 2020.

[14] K. P. Peppas, G. C. Alexandropoulos, E. D. Xenos, and A. Maras, "The Fischer–Snedecor $\mathcal{F}$-distribution model for turbulence-induced fading in free-space optical systems," *Journal of Lightwave Technology*, vol. 38, no. 6, pp. 1286–1295, Mar. 2020.

[15] G. Funes, M. Vial, and J. A. Anguita, "Orbital-angular-momentum crosstalk and temporal fading in a terrestrial laser link using single-mode fiber coupling," *Optics Express*, vol. 23, no. 18, pp. 23 133–23 142, 2015.

[16] C. Chen and H. Yang, "Characterizing the statistical distribution for transmission coefficient of turbulent optical orbital-angular-momentum channels," *Optics Express*, vol. 27, no. 20, pp. 28 968–28 982, Sep. 2019.

[17] E. Amhoud, B. S. Ooi, and M. Alouini, "A unified statistical model for atmospheric turbulence-induced fading in orbital angular momentum multiplexed FSO systems," *IEEE Transactions on Wireless Communications*, vol. 19, no. 2, pp. 888–900, Feb. 2020.

[18] M. Alfowzan, J. A. Anguita, and B. Vasic, "Joint detection of multiple orbital angular momentum optical modes," in *2013 IEEE Global Communications Conference (GLOBECOM)*. IEEE, Dec. 2013, pp. 2388–2393.

[19] C. Chen and H. Yang, "Characterizing the radial content of orbital-angular-momentum photonic states impaired by weak-to-strong atmospheric turbulence," *Optics Express*, vol. 24, no. 17, pp. 19 713–19 727, Aug. 2016.

[20] Y. Zhang, P. Wang, L. Guo, W. Wang, and H. Tian, "Performance analysis of an OAM multiplexing-based MIMO FSO system over atmospheric turbulence using space-time coding with channel estimation," *Optics Express*, vol. 25, no. 17, pp. 19 995–20 011, Aug. 2017.

[21] E. Zedini, H. M. Oubei, A. Kammoun, M. Hamdi, B. S. Ooi, and M.-S. Alouini, "Unified statistical channel model for turbulence-induced fading in underwater wireless optical communication systems," *IEEE Transactions on Communications*, vol. 67, no. 4, pp. 2893–2907, Jan. 2019.

[22] L. Allen, M. W. Beijersbergen, R. J. C. Spreeuw, and J. P. Woerdman, "Orbital angular momentum of light and the transformation of Laguerre-Gaussian laser modes," *Physical Review A*, vol. 45, pp. 8185–8189, Jun. 1992.

[23] A. Forbes, A. Dudley, and M. McLaren, "Creation and detection of optical modes with spatial light modulators," *Advances in Optics and Photonics*, vol. 8, no. 2, pp. 200–227, Jun. 2016.

[24] L. C. Andrews and R. L. Phillips, "Laser beam propagation through random media." SPIE, 2005.

[25] M. Charnotskii, "Sparse spectrum model for a turbulent phase," *Journal of The Optical Society of America A*, vol. 30, no. 3, pp. 479–488, Mar. 2013.

[26] V. Nikishov and V. Nikishov, "Spectrum of turbulent fluctuations of the sea-water refraction index," *International journal of fluid mechanics research*, vol. 27, no. 1, pp. 82–98, Jun. 2000.

[27] N. Farwell and O. Korotkova, "Intensity and coherence properties of light in oceanic turbulence," *Optics Communications*, vol. 285, no. 6, pp. 872 – 875, Mar. 2012.

[28] R. Lane, A. Glindemann, J. Dainty *et al.*, "Simulation of a Kolmogorov phase screen," *Waves in random media*, vol. 2, no. 3, pp. 209–224, Aug. 1992.

[29] D. A. Paulson, C. Wu, and C. C. Davis, "Randomized spectral sampling for efficient simulation of laser propagation through optical turbulence," *Journal of The Optical Society of America B*, vol. 36, no. 11, pp. 3249–3262, Nov. 2019.

[30] L. Lu, Z. Wang, P. Zhang, C. Qiao, C. Fan, J. Zhang, and X. Ji, "Phase structure function and AOA fluctuations of plane and spherical waves propagating through oceanic turbulence," *Journal of Optics*, vol. 17, no. 8, p. 085610, Jul. 2015.

[31] Z. Wang, L. Lu, P. Zhang, C. Fan, and X. Ji, "Broadening of ultra-short pulses propagating through weak-to-strong oceanic turbulence," *Optics Communications*, vol. 367, pp. 95 – 101, May 2016.

[32] J. A. Anguita, M. A. Neifeld, and B. V. Vasic, "Turbulence-induced channel crosstalk in an orbital angular momentum-multiplexed free-space optical link," *Applied optics*, vol. 47, no. 13, pp. 2414–2429, May 2008.

[33] M. Charnotskii, "Comparison of four techniques for turbulent phase screens simulation," *Journal of The Optical Society of America A optics Image Science and Vision*, vol. 37, no. 5, pp. 738–747, May 2020.

[34] L. Lu, X. Ji, and Y. Baykal, "Wave structure function and spatial coherence radius of plane and spherical waves propagating through oceanic turbulence," *Optics Express*, vol. 22, no. 22, pp. 27 112–27 122, Nov. 2014.

[35] Z. Wang, P. Zhang, C. Qiao, L. Lu, C. Fan, and X. Ji, "Scintillation index of Gaussian waves in weak turbulent ocean," *Optics Communications*, vol. 380, pp. 79 – 86, Dec. 2016.

[36] J. Martin and S. M. Flatté, "Intensity images and statistics from numerical simulation of wave propagation in 3-D random media," *Applied Optics*, vol. 27, no. 11, pp. 2111–2126, Jun. 1988.

[37] A. Belmonte, "Feasibility study for the simulation of beam propagation: consideration of coherent lidar performance," *Applied optics*, vol. 39, no. 30, pp. 5426–5445, Oct. 2000.

[38] M. Charnotskii, "Common omissions and misconceptions of wave propagation in turbulence: Discussion," *Journal of The Optical Society of America A*, vol. 29, no. 5, pp. 711–721, May 2012.

[39] C. Paterson, "Atmospheric turbulence and orbital angular momentum of single photons for optical communication," *Physical Review Letters*, vol. 94, p. 153901, Apr. 2005.

[40] A. Jeffrey and D. Zwillinger, *Table of integrals, series, and products*. Elsevier, 2007.

[41] J. Y. Wong, "Simultaneously estimating with ease the three parameters of the generalized gamma distribution," *Microelectronics Reliability*, vol. 33, no. 15, pp. 2233–2242, Dec. 1993.

[42] K. S. Song, "Globally convergent algorithms for estimating generalized gamma distributions in fast signal and image processing," *IEEE Transactions on Image Processing*, vol. 17, no. 8, pp. 1233–1250, Jun. 2008.

[43] E. W. Stacy, "A Generalization of the Gamma Distribution," *The Annals of Mathematical Statistics*, vol. 33, no. 3, pp. 1187 – 1192, Sep. 1962.

[44] E. Lukacs, "A characterization of the gamma distribution," *The Annals of Mathematical Statistics*, vol. 26, no. 2, pp. 319–324, Jul. 1955.

[45] A. W. Marshall and I. Olkin, "A multivariate exponential distribution," *Journal of the American Statistical Association*, vol. 62, no. 317, pp. 30–44, Apr. 1967.

[46] N. L. Johnson, "Systems of frequency curves generated by methods of translation," *Biometrika*, vol. 36, no. 1/2, pp. 149–176, Jun. 1949.

[47] A. A. Kilbas, *H-transforms: Theory and Applications*. CRC Press, 2004.

[48] A. Lapidoth, S. M. Moser, and M. A. Wigger, "On the capacity of free-space optical intensity channels," *IEEE Transactions on Information Theory*, vol. 55, no. 10, pp. 4449–4461, Sep. 2009.

[49] E. Zedini, H. Soury, and M.-S. Alouini, "Dual-hop FSO transmission systems over gamma–gamma turbulence with pointing errors," *IEEE Transactions on Wireless Communications*, vol. 16, no. 2, pp. 784–796, Nov. 2016.

[50] I. Gradshtein and I. M. Ryzhik, *Table of integrals, series, and products*. Academic Press, 2000.

[51] P. Mittal and K. Gupta, "An integral involving generalized function of two variables." Springer, 1972.